ELSEVIER

Journal of Atmospheric and Solar-Terrestrial Physics 68 (2006) 615–628

Journal of ATMOSPHERIC AND SOLAR-TERRESTRIAL PHYSICS

www.elsevier.com/locate/jastp

Realistic magnetospheric density model for 29 August 2000

R.E. Denton[a,*], J. Goldstein[b], D.-H. Lee[c], R.A. King[d], Z.C. Dent[e], D.L. Gallagher[f], D. Berube[g], K. Takahashi[h], M. Nose[i], D. Milling[e], F. Honary[j]

[a]*Department of Physics and Astronomy, Dartmouth College, 6127 Wilder Lab, Hanover, NH 03755, USA*
[b]*Space Science and Engineering Division (15), Southwest Research Institute, 6220 Culebra Rd., San Antonio, TX 78238, USA*
[c]*Department of Astronomy and Space Science, Kyung Hee University, Yongin, Kyunggi-Do, 449-701, Republic of South Korea*
[d]*University of Arizona, 901 GS LPL West, 1040 E 4th St., Tucson, AZ 85721, USA*
[e]*Department of Physics, Space Physics Group, University of Alberta, Edmonton, Alb., Canada T6G 2J1*
[f]*NASA Marshall Space Flight Center, 1321 Shadow Ridge Rd., Huntsville, AL 35803, USA*
[g]*UCLA, 595 Charles Young Dr East, 3806 Geology Bldg., Los Angeles, CA 90095-1567, USA*
[h]*Applied Physics Lab, Johns Hopkins University, 11100 Johns Hopkins Rd., Laurel, MD 20723-6099, USA*
[i]*Data Analysis Ctr. Geomagnetism & Space, Kyoto University, Oiwake-cho Kitashirakawa Sakyo-ku, Kyoto, 606-8502, Japan*
[j]*Department of Communication Systems, University of Lancaster, Lancaster LA1 4YR, Great Britain*

Received 22 February 2005; received in revised form 3 November 2005; accepted 24 November 2005
Available online 24 January 2006

Abstract

Using a two dimensional image of the Earth's plasmasphere taken by the Extreme Ultraviolet Imager (EUV) on the Imager for Magnetopause-to-Aurora Global Exploration (IMAGE) spacecraft, in-situ electron density measurements from the IMAGE Radio Plasma Imager (RPI) instrument, measurements of magnetospheric mass density inferred from field line resonant frequencies measured by magnetometers on the Earth's surface, and a model for the density field aligned variation, we construct a computer model for the magnetospheric density on 29 August 2000 at 1519 UT. The purposes of this study are to demonstrate how a density model can be constructed using multiple data sources, to document this particular model, which is being used in studies of ultra low frequency Pi-2 oscillations and plasmaspheric cavity modes, to describe some of the problems involved with EUV density inversion, and to demonstrate some features of the plasmaspheric density, particularly in the region of the dusk plasmatrough and plume.

Keywords: Plasmasphere; Density model; Mass density; Electron density; IMAGE EUV; Field line resonance mode

1. Introduction

The plasmasphere is the region of large plasma density surrounding the Earth (Wolf, 1995). It typically extends several Earth radii out from the Earth's surface along the magnetic equator, and the plasmaspheric density extends along the Earth's dipole field lines toward the magnetic poles. Recently, the Extreme Ultraviolet Imager (EUV) on the Imager for Magnetopause-to-Aurora Global Exploration (IMAGE) spacecraft has been able to image the ultraviolet emission of plasmaspheric helium (Sandel et al., 2001). Ideally, one would use

*Corresponding author. Tel.: +1 603 6462732; fax: +1 603 6461446.
E-mail addresses: richard.e.denton@dartmouth.edu, rdelsevier@rdenton.fasten.com (R.E. Denton).

1364-6826/$ - see front matter © 2005 Elsevier Ltd. All rights reserved.
doi:10.1016/j.jastp.2005.11.009

these images to extract a map of magnetospheric density. So far, such a task has been difficult. Difficulties relate to the relation of emission to local density, the line of sight integration of the emission, lack of emission at low density, and uncertainties about the field line distribution of density and the relative density of various plasma species. Here, we generate a computer model for the magnetospheric electron density and mass density at 29 August 2000, 1519 UT, by supplementing the EUV data with in-situ electron density measurements at earlier and later times (Bauer and Stone, 1968; Benson et al., 2004), and with mass density values inferred from field line resonance frequencies measured by magnetometers on the Earth's surface (Menk et al., 1999). We supplement these observations with a model for the field line dependence based on observations of electron density by the Polar spacecraft (Denton et al., 2002b, 2004, 2006).

The mass density controls the rate of response of the magnetosphere to MHD-scale internal or external perturbations. The purpose of this particular study is to derive a realistic mass density model to study the propagation of fast/magnetosonic magnetohydrodynamic waves through the plasmasphere and the resonance properties of these waves within the plasmaspheric cavity. (The waves may resonate within the plasmasphere much like sound waves resonate in a musical instrument.) A previous event study using a two dimensional model of the plasmasphere found that the plasmaspheric cavity resonance could account for the observed ultra low frequency (ULF) frequencies of Pi-2 oscillations of the Earth's magnetic field (Denton et al., 2002a). However, this study did not address the effects of a realistic three dimensional density model on the waves. Using the density model described here, Kim et al. (2005) have calculated the theoretical cavity mode frequency, and found that it was too low to account for Pi2 oscillations observed at 29 August 2000, 1520 UT. A model such as this one can also be useful for dynamics studies. Our current plans are to use this model to simulate the flow of energy around an asymmetric plasmasphere. Furthermore, this study also sheds new light on the distribution of magnetospheric density in certain regions, particularly in the region of the dusk plasmatrough and plume.

2. Development of the model

2.1. EUV image

The IMAGE EUV instrument images solar EUV photons at 30.4-nm wavelength that are resonantly scattered by singly ionized helium in the plasmasphere with a resolution of about 0.1 R_E from apogee (Sandel et al., 2001). The 30.4-nm feature is relatively easy to measure because it is the brightest ion emission from the plasmasphere, it is spectrally isolated, and the background at that wavelength is negligible. The plasmaspheric He+ emission is optically thin, so its brightness is directly proportional to the He+ column abundance. Full images are taken with at least 10 min resolution.

The IMAGE spacecraft has a meridional orbit (orbit over the poles). Fig. 1a shows the plasmaspheric image taken at 29 August 2000, 1519 UT,

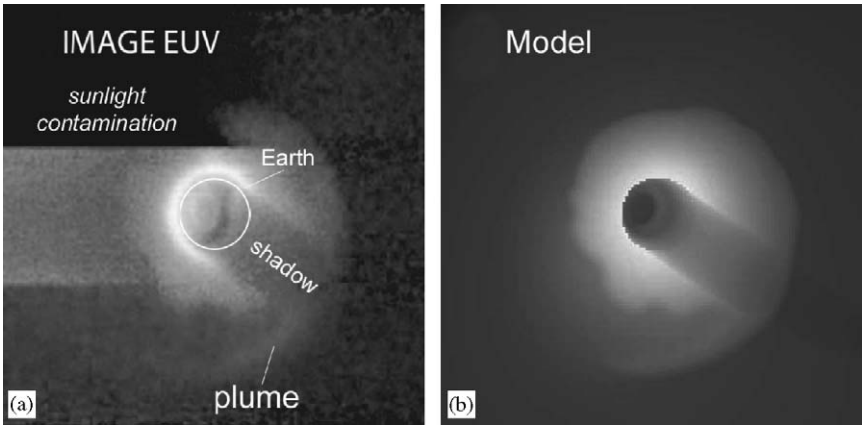

Fig. 1. (a) EUV instrument image of resonantly scattered solar EUV photons (30.4 nm) at 29 August 2000 1519 UT. (b) Simulated EUV instrument image using the model for electron density developed in this paper.

when the spacecraft was near its apogee over the North pole. The Sun is off the plot in the direction of the upper left corner; on the lower right side of the plot there is darker emission due to the Earth's shadow. The image is a composite from three cameras; this is the cause of the horizontal discontinuities in brightness. There is significant sunlight contamination on the left side of the plot, particularly for the middle camera. Much of the field of view of the upper camera is shielded to avoid damage to the camera. The increasing brightness toward the center of the image corresponds to higher density in the plasmasphere. The brightest (horseshoe shaped) ring comes from emission close to the surface of the Earth. (This emission is actually a combination of He+ emission other than 30.4-nm and O+ emission that is so bright that it is detected by EUV (Bill Sandel, private communication, 2004).) Considerable structure in the shape of the plasmasphere is evident; note particularly the plasma plume (or tail) at the bottom of the plot and curving around toward the left side of the plot.

Fig. 2 shows Kp and Dst during the ten days leading up to the time of our model. About a day earlier than August 2000, 1519 UT, there was a significant increase in Kp. Such an increase in activity is correlated with increased magnetospheric convection, which can erode the outer plasmasphere and lead to plasmaspheric plumes (Sandel et al., 2003). While there was a drop in Dst, that has largely recovered by August 2000, 1519 UT.

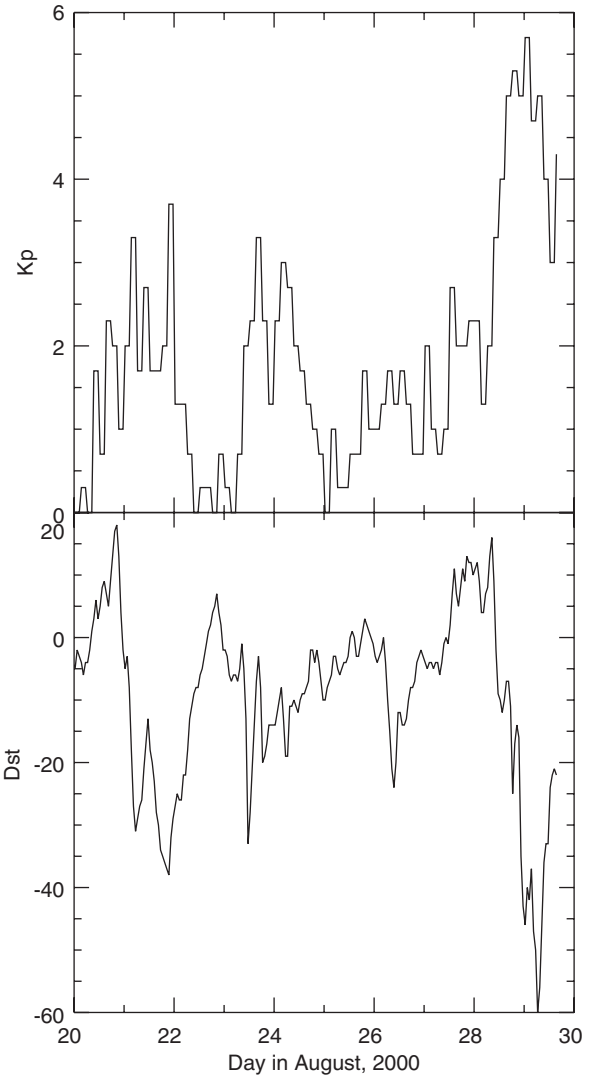

Fig. 2. Kp from August 20 to August 29.

2.2. Plasmapause position

The plasmapause is the outer boundary of the high density plasmasphere where the density falls off steeply. (The plasmapause is not always steep or obvious (Carpenter and Anderson, 1992; Denton et al., 2004), but is clear at the time we are considering.) The region outside the plasmasphere is called the plasmatrough. In Fig. 1a, there is an irregular boundary where the 30.4-nm emission falls off sharply. Goldstein et al. (2003) calls this the "He+ edge", and shows that this visual feature corresponds to the location of the plasmapause (sudden drop in electron density). This drop in bright emission may and often does cross an EUV instrument threshold $\sim 40 \pm 10\,\mathrm{cm}^{-3}$.

The asterisks in Fig. 3 show the plasmapause determined using the method of Goldstein et al. (2003), which maps the observed position of the plasmapause to the magnetic equator using the dipole field model. The image of Fig. 1a has now been rotated into Solar Magnetic (SM) coordinates, with X in the direction of the Sun (toward the left of the plot), and Y in an eastward direction (toward the bottom of the plot). Thus the Sun is to the left in Fig. 3. The half illuminated circle at the center of the plot shows the location of the Earth. The location of the plasmapause at local noon (facing the Sun) is not indicated by asterisks in Fig. 3 because the corresponding region of the image in Fig. 1a is blacked out to protect the camera.

The solid curve in Fig. 3 shows the location of the plasmapause used in the model. The plasmasphere rotates with the Earth in a counterclockwise direction (viewing the Earth from above the north

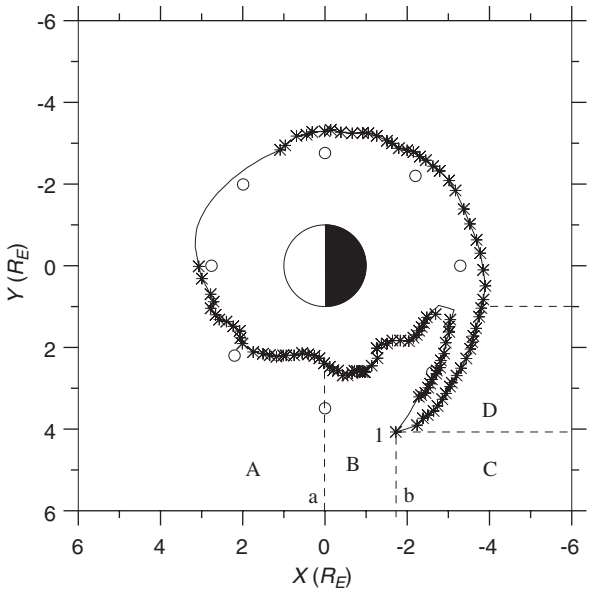

Fig. 3. Plasmapause position in SM coordinates X and Y in units of Earth radii R_E. The asterisks show the plasmapause determined using the method of Goldstein et al. (2003). The solid curve shows the plasmapause used in the model. The open circles show the position of the plasmapause model of Moldwin et al. (2002). The regions A, B, C, and D, lines a and b, and point 1 are discussed in Section 2.5.

pole). The rotation of the plasmasphere is usually close to the Earth's rotation rate (Wolf, 1995; Sandel et al., 2003; Burch et al., 2004). Thus by looking at the plasmapause at dawn in earlier EUV instrument images or at dusk in later ones, we may be able to get an idea of the plasmapause structure at 1519 UT (time corresponding to Fig. 1a) at local noon. (As a caution, Laakso and Jarva (2001) show that the plasmapause shape and position can change quite rapidly, so this method might not work in general.) Using EUV images before and after 1519 UT, no large amount of structure was observed for this region, so we connected the measured plasmapause positions at early morning local time to that in at early afternoon local time with a roughly radial connection. A slight bulge in the plasmapause was included at magnetic local time MLT ~10.7 to bring the plasmapause out to $L = 3.2$ at that local time (see discussion in Section 2.5). A smooth connection of the asterisks was also made in the plasma plume. For comparison, the open circles in Fig. 3 show the plasmapause model of Moldwin et al. (2002) for Kp_{max} (maximum Kp in the preceding 24 h) = 5.75 (Fig. 2). (Note that the database of Moldwin et al., 2002 includes plasmapause positions corresponding to the outer edge of the plume as indicated by Fig. 1b.)

2.3. Electron density in the inner plasmasphere

The IMAGE spacecraft was near its apogee at 1519 UT when the image in Fig. 1a was taken. After 1519 UT, the spacecraft moved toward MLT~2.5 (post-midnight) as it approached perigee at a height of 1.2 R_E. It then passed at low altitude over the South pole and moved outward at MLT~13.7 (afternoon). Because of this, IMAGE passed through the plasmasphere at two MLT values within 8–11 h UT after 1519 UT. Similarly, IMAGE passed through the plasmasphere at two different MLT values within 3–6 h UT before 1519 UT.

The Radio Plasma Imager (RPI) instrument on IMAGE (Reinisch et al., 2000), when operated in its passive mode, measures (among other emissions) emission which is associated with the upper hybrid frequency, and the frequency of this emission can be used to infer the local electron density n_e (Bauer and Stone, 1968; Benson et al., 2004). Values of the equatorial electron density n_{e0} determined before and after 1519 UT are shown in Figs. 4a–d for the four UT and MLT values indicated in each panel. The equatorial values are obtained by using the electron density field line dependence described in Section 2.9. (Both the UT and MLT values are typical values approximating a range of values. Figs. 4b and d plot the density values for consecutive time values near spacecraft perigee where L first decreases, then increases; that is why the L values are not monotonic.) The MLT values are shown in the format $MLT_1 \rightarrow MLT_2$. The first value MLT_1 is the local MLT where the measurements were taken, and MLT_2 is the value of MLT mapped from MLT_1 to the MLT value at 1519 UT (MLT_2) assuming corotation. For instance, the measurements of n_e in Fig. 4b were measured at 11.5 UT at MLT = 14.8. This is 3.8 h UT earlier than 1519 = 15.3 UT. Assuming then that the plasma observed in Fig. 4b corotated with the Earth from 11.5 to 15.3 (1519) UT, it would have moved from $MLT = MLT_1 = 14.8$ to $MLT = MLT_2 = 14.8 + 3.8 = 18.6$ by 1519 UT.

The data in Figs. 4a–d could be used to get the electron density at various MLT values, but it is not clear which MLAT values to use, the instantaneous or mapped values. Fortunately, we did not need to make such a choice, because the plasmaspheric data lies fairly close to a single line, as shown in

Fig. 4e. The data at all four times is superposed in Fig. 4e. While there is a significant variation in the low density values with $n_e < 40\,\mathrm{cm}^{-3}$ (plasmatrough), the high density values (plasmasphere) fit fairly well on the dashed line

$$\log_{10}(n_e) = 5.25 - 0.82L \quad (1)$$

from about $L = 1.4$ to 3.4. With a slight modification (described in Section 2.4), we use Eq. (1) to describe n_e within $L = 3.2$.

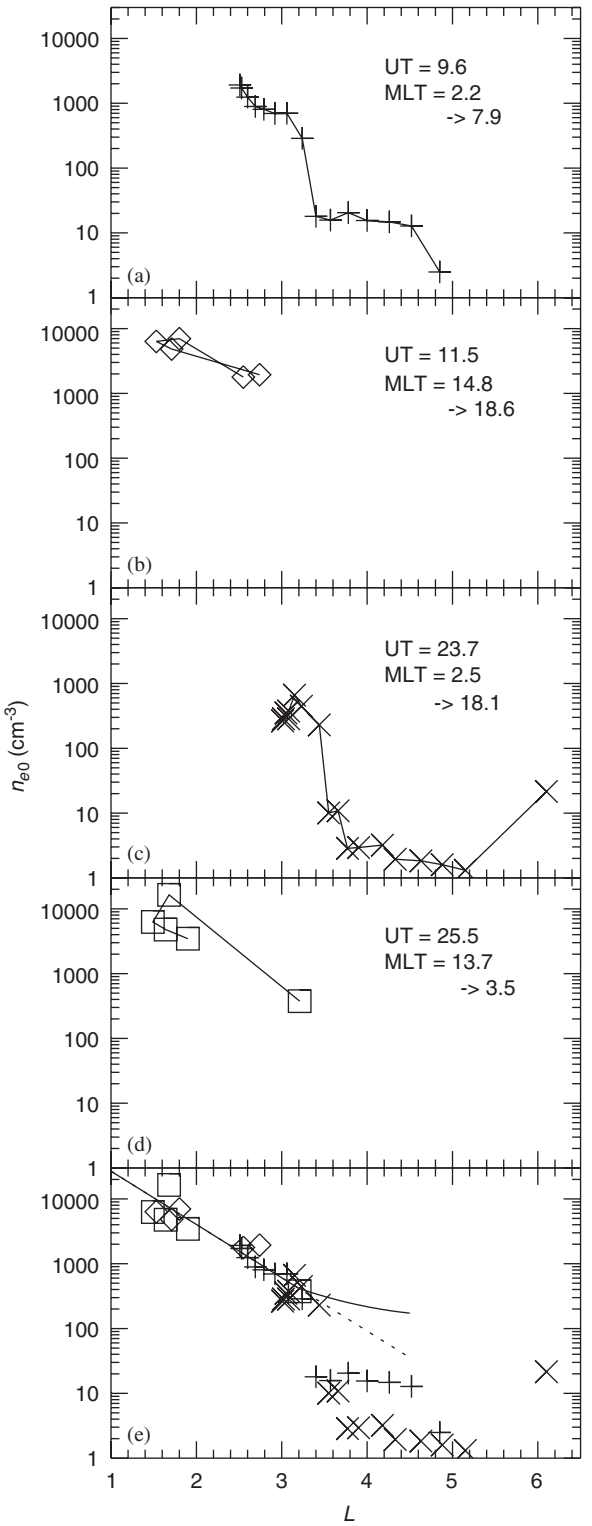

Fig. 4. (Equatorial electron density n_{e0} versus L as measured by IMAGE RPI at universal times close to the values indicated in each panel. The two MLT values given in each panel in the format $\mathrm{MLT}_1 \rightarrow \mathrm{MLT}_2$ are the MLT value where n_e was measured (MLT_1) and the value of MLT mapped from MLT_1 to the MLT value at 1519 UT (MLT_2) assuming corotation. (e) All the measurements superposed.

2.4. MLT dependence in the inner plasmasphere

A code has been developed to invert the EUV instrument image and get a "pseudo-density" of He+, n_{He}. Counts are first translated into integrated column density using the SOLAR2000 solar flux model (Tobiska et al., 2000). The assumption is made that the plasmaspheric densities drop rapidly with L-shell and that the dominant contribution to image intensity in any single pixel comes from that portion of the line of sight that passes within $0.1\,L$ of the minimum L-shell. The length of that segment in the line of sight increases with increasing L-shell for an observing location at high latitude and can result in a bias toward larger L-shell of as much as a factor of three. Column density in cm^{-2} is converted to density in cm^{-3} by dividing by the length of that segment of the line of sight. See (Gallagher et al., 2005) for further description of the algorithm.

Density structure is fairly well ordered by the Earth's magnetic field, which is approximately dipolar. In three dimensions, the density structures evident in the equatorial plane (structures similar to, but not exactly the same as those shown in Fig. 1a) drape up out of the equatorial plane along magnetic field lines and turn down toward the poles. The calculation of pseudo-density does not take into account overdraped field line content (high density at large L that because of the shape of the magnetic field drapes across the field of view looking toward a lower L in the equatorial plane). That means that low pseudo-densities radially inward of a density enhancement (especially the plume) would be expected to be somewhat higher than the actual density.

Fig. 5 shows a greyscale plot of the log of the He+ pseudo-density n_{He} using Fig. 1a as an input. Fig. 6 shows the pseudo-density n_{He} versus L at four different values of MLT, MLT = 18 (thin solid curve), 21 (thick solid curve), 3 (small dashed curve), and 6 (large dashed curve). From the pseudo-density, we can see several features of the plasmasphere, a steeply dropping density within the plasmasphere proper (i.e., within $L \leqslant 3$), a drop to a much lower density at large L (except for MLT = 18), and the plasma plume (bump in the thick solid curve at $L \sim 3.8$).

Ideally, we would just use the density plotted in Figs. 5 and 6 and multiply by the electron to He+ ion ratio to get the electron density. However, the uncertainties in the method leading to Fig. 5 are too great to follow that procedure. If we assume a constant n_e/n_{He} ratio, the densities in Fig. 5 are not consistent with the data presented elsewhere (for instance, Fig. 7). If we use the Craven et al. (1997) model for n_e/n_{He}, the disagreement is worse, as we explain in Sections 3.2 and 3.3. Because of this, we use a constant n_e/n_{He} ratio in our model and we use

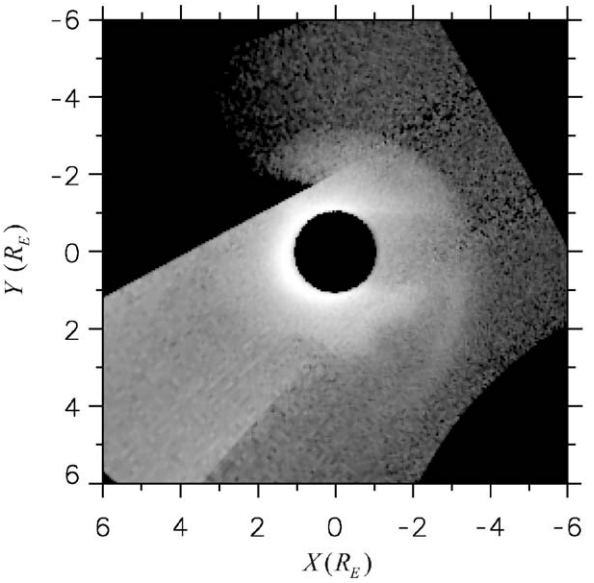

Fig. 5. Grayscale plot of the log of the pseudo-density of He+, n_{He}, in the equatorial plane versus SM coordinates X and Y using Fig. 1a as an input.

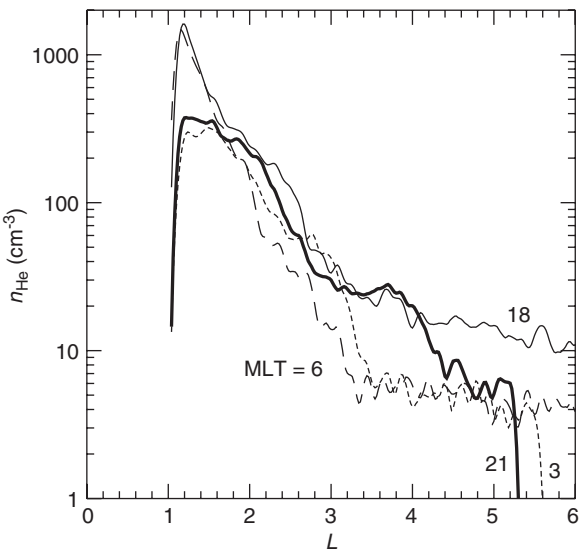

Fig. 6. Pseudo-density of He+, n_{He}, versus L along four cuts, MLT = 18 (thin solid), 21 (thick solid), 3 (small dashes), and 6 (large dashes).

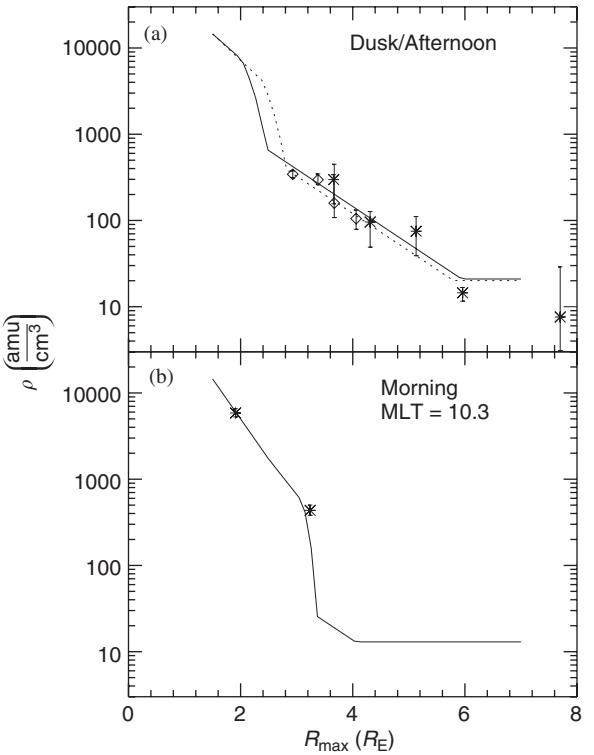

Fig. 7. (a) Inferred mass density at UT~1519 (time of EUV image in Fig. 1a) in the vicinity of the magnetic equator versus L based on field line resonance frequencies measured by Scandinavian meridian ground magnetometers (asterisks) at MLT~17.6 and by UK meridian ground magnetometers (diamonds) at MLT~15.8, and our model mass density at MLT = 17.6 (solid curve) and at MLT = 15.8 (dashed curve). (b) Inferred mass density based on frequencies measured by MEASURE ground magnetometers (asterisks) at MLT~10.3, and our model mass density at MLT = 10.3 (solid curve).

the pseudo-density as a guide for some limited aspects of the model.

First we note that the density in the inner plasmasphere ($L \leqslant 3.2$) has a small MLT dependence. The solid curves in Fig. 6, representing density on the duskside, are somewhat higher than the dashed curves, representing the density on the dawn side. We incorporate this into the model by modifying Eq. (1) as follows:

$$\log_{10}(n_e) = 5.25 - 0.82L + 0.25(L - 1.5) \times \cos(2\pi(\mathrm{MLT} - 18)/24), \quad (2)$$

where MLT is given in hours. (Beyond $L = 2.5$, the $L - 1.5$ term is replaced by unity. Therefore, the maximum MLT variation is a factor of $10^{0.25} = 1.8$.) The exact dependence given here is just a qualitative approximation to the general dependence seen in Fig. 6.

The second observation is that the density in the plume (peak in the thick solid curve (corresponding to MLT = 21) at $L = 3.8$ in Fig. 6) is larger than one would expect based on the dropoff in density up to about $L = 3$. That is, if you were to fit a straight line to the thick solid curve in Fig. 6 between about $L = 1.8$ and 3.0, that straight line would pass well below the plume density at $L = 4$. Because of this, our plasmasphere density (solid curve in Fig. 4e) decreases less strongly outside $L = 3.2$ than it would if we simply extended the straight line fit curve in Fig. 4e (dashed line in Fig. 4e). An even stronger motivation for the choice of the outer ($L > 3.2$) plasmaspheric density is discussed in Section 3. Basically, the plume density must be greater than that indicated by the extension of a straight line in Fig. 4e (dashed line in Fig. 4e) because such an extension would make the density lower than the density of the region around the plume (enhanced plasmatrough density described in Section 2.5). The plasmasphere density for $L > 3.2$ is

$$\log_{10}(n_e) = 2.62 - 0.45(L - 3.2) + 0.12(L - 3.2)^2 + 0.25\cos(2\pi(\mathrm{MLT} - 18)/24). \quad (3)$$

Eq. (3) yields a density which connects smoothly to (2) at $L = 3.2$, gradually decreases (in accordance with the decreasing brightness of the plasmasphere component in Fig. 1), and still lies above the enhanced plasmatrough component described in Section 2.5. (The exact dependence is simply a convenient numerical form.)

2.5. Mass density based on field line resonance frequencies

The field line resonance mode is an azimuthally oscillating (toroidal) Alfven wave. The resonance frequency is particularly dependent on the mass density in the vicinity of the magnetic equator, where the magnetic field strength is a minimum (Denton and Gallagher, 2000). Given a realistic magnetic field model, the magnetospheric mass density in the vicinity of the magnetic equator can be determined from field line resonance frequencies measured by magnetometers on the Earth's surface. Here we use data from the SAMNET (Sub-Auroral Magnetometer Network, http://www.dcs.lancs.ac.uk/iono/samnet/, Yeoman et al., 1990), IMAGE (International Monitor for Auroral Geomagnetic Effects, http://sumppu.fmi.fi/image/, Luhr et al., 1998), BGS (British Geological Survey, data available from SAMNET) ground magnetometer arrays in Europe and Antarctica, and from the MEASURE (Magnetometers Along the Eastern Seaboard for Undergraduate Research, http://measure.igpp.ucla.edu/, Berube et al., 2003) ground magnetometer array. The resonant field line was determined using the cross phase technique with pairs of stations (Waters et al., 1991).

For each measurement, the T96 magnetic field model (Tsyganenko, 1995) is used to map the ground station location to the equatorial plane where the magnetic field is a minimum. The normalized frequency of the Alfven wave fundamental $\bar{f}_1 \equiv f_1 L R_E / V_{A-B\,\mathrm{min}}$ is calculated using the dipole field model (as described by Schulz, 1996 or Denton and Gallagher, 2000), but for $LR_E = R_{B\,\mathrm{min}}$, where $R_{B\,\mathrm{min}}$ is the geocentric radius to the point on the field line where B is minimum according to the T96 model, and $V_{A-B\,\mathrm{min}}$ is the Alfven speed at that location. A perfect conductor boundary is assumed at a height of 400 km above the ground. (A more realistic height would be about 70 km, suggested by Fig. 3 of Hughes and Southwood (1976), or perhaps 100–120 km, theusual peak of the Pederson conductivity. Fortunately, these assumptions lead to only a small difference in the inferred mass density of order 3%.) For the field line dependence, ρ is assumed to vary along field lines like $R^{-0.5}$, where R is the geocentric radius, based on results by Takahashi et al. (2004). (We will assume somewhat a different dependence for the electron density, as discussed in Section 2.9. The field line dependence may actually be different for mass and

electron density (Denton et al., 2006). At any rate, the difference in the inferred equatorial mass density based on an $R^{-0.5}$ field line dependence or the dependence described in Section 2.9 is only about 10% (Denton et al., 2006).)

The normalized frequency is not a strong function of L except at very low $L \leqslant 2$. Except for the point with $R_{B\min} = 1.9R_E$, for which $\bar{f}_1 = 0.42$, $\bar{f}_1$ is equal to 0.35 ± 0.02 for all our data points. Then, from the definition of the normalized frequency, the mass density at the magnetic equator (in amu/cm^3) is found from

$$\rho = \left(\frac{3.42 B_{\min} \bar{f}_1}{G R_{B\min} f_1}\right)^2, \quad (4)$$

where f_1 is in mHz, and $B_{\min}$ (in nT) and $R_{B\min}$ (in R_E) are found from the T96 model, and G is the ratio of the total length of the T96 field line to that of a dipole field line with $LR_E = R_{B\min}$ (G is within 8% of unity for all our data points). Using the values of $B_{\min}$ and $R_{B\min}$ from the T96 magnetic field in this way results in a more accurate estimate of ρ than would be found from the dipole field model alone.

After the density model was developed, we tested the accuracy of (4) by solving Singer et al. (1981) wave equation directly, and adjusting ρ so that the theoretical frequency matched the observed frequency f_1 (Takahashi et al., 2006). The resulting ρ values based on the frequencies used in this paper were an average of 7% higher than the values given by (4) with an additional spread (standard deviation) of 5%. On the other hand, if we mapped the dipole field to the equator to get $B_{\min}$ and $R_{B\min}$ (with $G = 1$), the resulting ρ values were on an average factor of 3.5 off from the values found from the Singer et al. (1981) equation. These results are consistent with those of Singer et al. (1981), who showed that frequencies found using a dipole magnetic field (labelled by L) were a poor approximation to those found using the Olson–Pfitzer magnetic field model if L was defined based on invariant latitude, but they agreed fairly well if L was defined as the radius at the equatorial crossing of the field line. We also tested (4) on our dataset of f_1 values measured by the CRRES spacecraft (Takahashi et al., 2006). In this case, the observations were relatively close to the magnetic equator, and there was no advantage in using the T96 values in (4) compared to using the dipole field values. Based on these tests, the most important factor for an accurate solution of the inferred ρ is to use a realistic value of $R_{B\min}$, and a magnetic field value that is consistent with $R_{B\min}$ (whether based on a dipole magnetic field model or on some other model).

Fig. 7a shows mass density values inferred from field line resonance mode frequencies at dusk local time, MLT~17.6 (asterisks, Scandinavian meridian) and 15.8 (diamonds, UK meridian). Fig. 7b shows two inferred mass density values at morning local time, MLT~10.3 (asterisks, MEASURE). Unlike the data shown in Fig. 4, these density values are based on measurements at UT~1519 (time of EUV image in Fig. 1a). The curves in the plots represent the mass density from our model. Within the plasmasphere ($L \lesssim 2.2$ in Fig. 7a and $L \lesssim 3.2$ in Fig. 7b), the model is determined by the electron density in (2) with an assumed average ion mass of 1.4 amu throughout the magnetosphere. This factor gives rough agreement between the plasmaspheric mass density values at dawn (Fig. 7b)and the RPI local electron density values (Section 2.3), as indicated by the agreement of the asterisks and solid curve in Fig. 7b. (For further discussion concerning the average ion mass, see Sections 3.2 and 3.3.)

Based on the mass density values in Fig. 7a, we include in our model a region of enhanced density concentrated in the dusk local time sector and outside the plasmasphere proper (outside L~2.5 at MLT = 18). Based on the radial dependence in Fig. 7a, we model this density as

$$\log_{10}(n_e) = 3.75 - 0.43L. \quad (5)$$

As can be seen from Fig. 7a, the density in this region falls off less steeply with respect to L than does the density in the plasmasphere at $L \leqslant 2.4$. Eq. (5) describes the density in region B of Fig. 3. This density component also contributes to the density in regions A, C, and D of Fig. 3; however, in these regions the density in Eq. (5) is multiplied by a factor that decreases with respect to the distance away from region B. As can be seen from Fig. 1, the EUV emission from the region outside the plasmasphere in region B falls off in the other regions, particularly toward midnight local time. Based on this fact, and the general expectation that there would be some accumulation of plasmatrough density in the afternoon local time sector due to the convective pattern, we chose a small spatial scale, 1 h, for the falloff of the density toward midnight, but a larger spatial scale, 5 h, for the

falloff of the density toward noon. These spatial scales were simply reasonable guesses. As mentioned in Section 3.3, the pseudo-density from the EUV inversion does not give much useful information about the MLT dependence of this dusk plasmatrough density component. To implement this falloff in the model, in region A, the density in Eq. (5) is multiplied by $\exp(-((18-\mathrm{MLT})/5)^2)$; in region C, the density in Eq. (5) is multiplied by $\exp(-(X_1-X)^2)$, where X_1 is the X coordinate of point 1 in Fig. 3; and in region D, the density in Eq. (5) is multiplied by $\exp(-((X_1-X)^2+(Y_1-Y)^2))$, where Y_1 is the Y coordinate of point 1 in Fig. 3. This component models the density from $L=2.4$–6 in Fig. 7a. Based on the last inferred density at $L=7.6$, it would have been better to have extended this component to lower densities; that is, the floor (low constant density at high L in Fig. 7) mentioned in Section 2.6 might have been chosen lower.

For the outer measurement at $L\sim3.2$ in Fig. 7b, the phase relation between the waves measured by the two ground magnetometer stations used (with the cross phase technique: see (Waters et al., 1991)) was reversed from the normal relation, indicating that the L value might be within the plasmapause (Menk et al., 1999). For this reason, we made the model plasmapause (Fig. 3) bulge out slightly at MLT$\sim$10.3 to put that data point near the model plasmapause (Fig. 7b). Note that we have no data from EUV at this local time.

2.6. Floor on the electron density at large L

Fig. 4e shows that there is a large variation in the electron density at large L in the region outside the plasmasphere. Values range from 1 to 20 cm^{-3} at the times indicated in Fig. 4e. The EUV image shows a significant amount of light at large L in the original EUV image (though not enough to be usually identified with the plasmasphere), indicating that the density at large L may be a significant fraction of 40 cm^{-3}, the density typically associated with the EUV plasmasphere threshold (Goldstein et al., 2003, 2004). (Other factors, such as solar EUV flux level and activity level affect this threshold, but 40 cm^{-3} is a reasonable estimate of the value.) Because of this, we put a floor (lower limit) on n_e near the upper limit of 1–20 cm^{-3} range observed by RPI (Fig. 4e), $(11+4\cos(2\pi(\mathrm{MLT}-18)/24))$ cm^{-3}. The MLT variation, leading to a factor of two greater value for the density floor at dusk than at dawn, was motivated by the presence enhanced plasmatrough density at dusk (Fig. 7), the apparently larger plasmatrough density at larger L in the cuts of pseudodensity (Fig. 6), and the relative brightness of the dusk and dawn regions in the original image (Fig. 1a). However, the exact form of this density component is just a reasonable guess. Note that a factor of two difference in plasmatrough density is roughly consistent with the higher density found by Carpenter and Anderson (1992) at MLT = 9–15 as compared to 0–5 (Fig. 5 of their paper).

2.7. Plasmapause width

We included in the model a variation of the plasmapause width, motivated by the apparent relative sharpness of the plasmapause in the original image at dawn (Fig. 1a) relative to dusk. At dusk, the plasmasphere more diffusely blends into the region of enhanced plasmatrough density (channel between plasmasphere and plume). Note from Fig. 6 that the gradient scale length for MLT = 18 and 21 at about $L=2.8$ appears to be somewhat larger than that for MLT = 3 at $L=3.4$. We used a sinusoidal variation of the plasmapause width with respect to MLT. The maximum width is 0.4 R_E at MLT = 17 h, and the minimum width is 0.1 R_E at MLT = 5 h. These values represent an informed guess. Fig. 6 would suggest that larger values might be used, but tests of the pseudo-density inversion method indicate that the inferred plasmapause width may be somewhat larger (order 50%) than the real width. Note that a median plasmapause width from Carpenter and Anderson (1992) is 0.1–0.2 R_E. Note also that our choice for the MLT dependence is somewhat different from the dependence suggested by the statistical study of Carpenter and Anderson (1992). They suggest that the nighttime (region centered at midnight) plasmapause width is less than the daytime (region centered at noon) width. Within the plasmapause, the equatorial density varies linearly from the value in the plasmasphere to the value outside the plasmasphere (just a convenient numerical approximation).

2.8. Polar cap

Outside of $L=13$ (based on the dipole field model), we assume that we are in the polar cap. (Our emphasis in this model is the plasmasphere rather than the polar cap. The value of $L=13$ was chosen to yield a typical equatorial distance to the

dayside magnetopause. A more accurate description of this region would require a more accurate magnetic field model.) Within the polar cap, we model the electron density using the formula given by Gallagher et al. (2000),

$$\log_{10}(n_e) = -3.09\log_{10}(h) + 13.5, \quad (6)$$

where h is the altitude in km and n_e is the density in cm^{-3}.

2.9. Field line dependence

For the field line density variation, we used the model of Denton et al. (2002b, 2004, 2006) based on electron density measurements from the Polar spacecraft. Along the field line, a power law dependence is assumed with respect to the geocentric radius,

$$n_e = n_{e0}(LR_E/R)^{\alpha}, \quad (7)$$

where n_{e0} is the equatorial electron density. The value of α is given by

$$\alpha = \alpha_{\mathrm{model}} = 8.0 - 3.0\log_{10} n_{e0} + 0.28(\log_{10} n_{e0})^2 - 0.43L. \quad (8)$$

(There is no strong direct dependence on Kp, but the value of Kp may affect α_{model} through its effect on n_{e0} (Denton et al., 2002b, 2004).)

If this formula led to $\alpha<0$, we raised α to zero. Also, motivated partly by the results of Denton et al. (2004) (showing that the density at $R\sim2R_E$ often levels off at large L to $n_e\sim100\,\mathrm{cm}^{-3}$) and partly by the fact that low density at low altitude can cause numerical problems in simulations, we imposed an additional criterion on α. If the density at a radius of $2R_E$ based on Eq. (7) with Eq. (8) is less than $100\,\mathrm{cm}^{-3}$, α is increased so as to bring the density at $R=2R_E$ up to $100\,\mathrm{cm}^{-3}$.

For simplicity, we used the same field line dependence for mass density as for electron density. However, the reader should be aware that calculations of the field line dependence of mass density using field line resonance mode harmonics (Takahashi et al., 2004; Denton et al., 2006) indicate that the mass density might be better modelled using a low value of $\alpha=0$–1 throughout the entire (closed) magnetosphere. These calculations suggest that the mass density may be locally peaked at the magnetic equator at $L>6$ (where (8) yields $\alpha\sim2$–3). Thus in the vicinity of the magnetic equator, the mass density field line dependence may be more complicated than that suggested by (7). At higher latitudes, the mass density probably has a dependence similar to that of the electrons, except that at low altitudes (perhaps geocentric radius $R<2R_E$) there may be ionospheric mass loading.

3. Discussion

3.1. Summary of model

Our goal has been the generation of a mass density model that is realistic (accurate within perhaps a factor of 2) in the regions where we have good information about the density (plasmasphere proper and plasmatrough at dusk) and at least reasonable in the regions where our diagnostics are not so good (especially the outer plasmatrough). The first input to our model is the EUV image of resonantly scattered solar EUV photons at 29 August 2000 1519 UT (Section 2.1, Fig. 1a). This image provides the plasmapause boundary (Section 2.2, Fig. 3) and some evidence regarding the MLT dependence of density in the plasmasphere and density of the plume relative to the surrounding plasma (Section 2.4) and regarding the density in the plasmatrough at large L (Section 2.6). The local electron density measurements from IMAGE RPI (Section 2.3, Fig. 4) provide the electron density in the plasmasphere proper (plasmasphere excluding the plume) as a function of L and some guidance concerning the electron density in the plasmatrough (Section 2.6). The inferred mass density values from the field line resonant mode provide the average ion mass (assumed to be constant throughout the magnetosphere) and the density in the dusk region outside the plasmasphere (Section 2.5, Fig. 7). Fig. 8 shows the logarithm of the model equatorial density (either electron or mass density, since the grayscale levels are uncalibrated) as a function of SM coordinates X and Y.

From the equatorial density, we use the field line dependence model of Denton et al. (2002b) to generate a three dimensional model of magnetospheric electron and mass density. Using the model electron density as an input, a simulated EUV image is generated. The procedure is as follows. Line of sight vectors are calculated over a 151 by 151 grid of 0.6° pixels using IMAGE orbit and attitude data for the epoch (an EUV image is roughly 85° in a direction normal to the scan plane of the spacecraft and 360° in the transverse direction, and has pixels that are 0.6° to a side), and then the pixel line of sight integrated He+ 30.4-nm signal is estimated

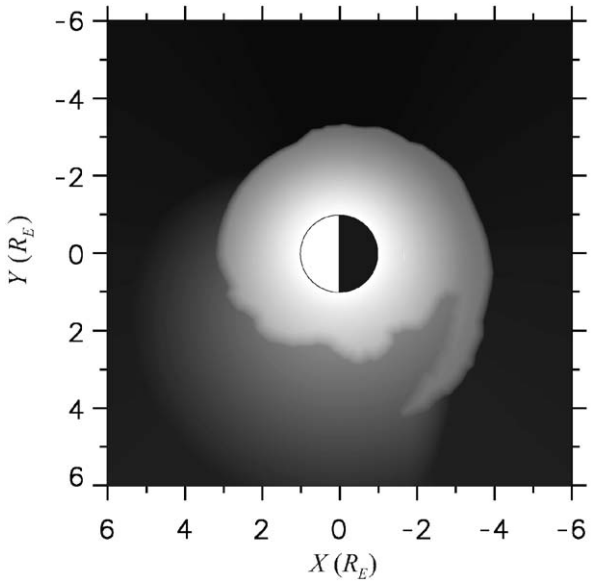

Fig. 8. Grayscale plot of the equatorial density as a function of SM coordinates X and Y.

under the assumption of a constant ratio of He+ to electrons. The numerical integration extends from the spacecraft out to $L = 9$ on the far side of Earth, excluding any part subtended by the Earth's shadow, and is simplified by the fact that although the volume of any voxel (three dimensional pixel) along the line of sight scales as r^2, where r is the distance to the voxel, the radiation collected by the sensor from that voxel falls as r^{-2}. The electron density within a voxel is taken to be the model electron density at its center.The simulation assumes a perfect detector and, up to a scale factor, should be consistent with EUV images that have been processed to remove geometric distortions and the effects of spacecraft rotation, and have been flat fielded and registered during ground processing.

The resulting image is shown in Fig. 1b. Though presented last, the comparison between Figs. 1a (real EUV image) and 1b (simulated EUV image using our density model) provided additional input to the model. For instance, based on the results from the simulated image the width of the plume was decreased where there was some uncertainty about the exact location of the outer edge, and the ratio of density in the plume relative to the slot region just inside the plume was increased. The general similarity of Figs. 1a and b provides support for the overall model.

3.2. Enhanced oxygen and the average ion mass

Observations by the DE-1 spacecraft showed that a region of enhanced O+ density may occur in the vicinity of the plasmapause (outer plasmasphere and the region of the plasmatrough outside but near to the plasmapause) (Horwitz et al., 1984; Roberts et al., 1987). Recently, Fraser et al. (2005) have stressed the effects that such a region of O+ enhancement can make on the mass density profile. In some cases, the contribution of O+ to the mass density can be so great that the mass density does not exhibit a steep drop in density with respect to L (plasmapause) even though there is such a drop in electron density. Note that Fig. 2 shows there was some significant activity preceding the time corresponding to our model, which could lead to enhanced levels of O+, though, on the other hand, Dst has largely recovered.

Our specific information about mass density comes from the inferred values plotted in Fig. 7. The first thing to note here is that we have very limited information about the mass density. The measurements are confined to two regions of local time, MLT~17.6 (Fig. 7a) and ~10.3 (Fig. 7b). Our main calibration of the average ion mass (ratio of mass density to electron density) is based on the inferred mass density at L~2 in Fig. 7b. That value is compared to the model electron density from (1) (or more precisely, (2)), which is predominantly based on the average plasmasphere electron density measured during several passes of the IMAGE spacecraft through the plasmasphere (Fig. 4e). Based on this comparison, the average ion mass is 1.4 amu. If the mass density is dominated by the H+ and He+ components, this implies that the ratio of He+ density to that of the electrons is $n_{He+}/n_e = 0.13$. This is consistent with the value from Eq. (4) of Craven et al. (1997) at $L = 2$, 0.12 (using their solar flux parameter $P = 170$).

Roberts et al. (1987) report that regions of O+ enhancement typically occur at $L > 2$ in a region surrounding the plasmapause. This could affect the interpretation of the second data point in Fig. 7b at $L = 3.2$. Recall that this data point involved a reversed phase relation which may indicate that it is within the plasmapause (Section 2.6). In Fig. 7b, this point occurs near the inner edge of the plasmapause (nearly in line with the model plasmasphere density). However, this local time sector was blacked out in the EUV image (Section 2.2). It is least possible, then, that the data point lies outside

of the plasmapause, and that the mass density is higher because of O+. However, the mass density was definitely not raised above that expected based on the plasmasphere L dependence, since the point at $L = 3.2$ in Fig. 7b is nearly in line with the model plasmasphere curve (solid curve in Fig. 7b). Furthermore, the phase measured in the cross phase technique indicates that this point may be within a region of steeply decreasing mass density.

Our other inverted mass densities are for MLT~17.6 (Fig. 7a). These mass densities are definitely below the values expected for the plasmasphere (below the extension of the solid curve at $L \leqslant 2$ in Fig. 7a), showing that a possible enhancement of the average ion mass due to O+ in this region, at least, does not bring the plasmatrough mass density up to plasmaspheric levels. Thus, while we cannot rule out an enhancement in the plasmatrough density, there does appear to be a drop in both electron and mass density at the plasmapause. We cannot be sure what the average ion mass is in the plasmatrough. It could well be that within the plasmatrough the average ion mass is greater than 1.4. Takahashi et al. (2006) suggest, for instance, that a typical value of the average ion mass in the plasmatrough may be about 3 amu. Besides the average ion mass, we do not really know the exact level of the plasmatrough density or radial or azimuthal dependence, however, our primary emphasis has been on the structure of the plasmasphere, and the observations do indicate that there is a drop in mass density (Fig. 7) as well as electron density (Fig. 4) at the plasmapause.

3.3. Comparison of pseudo-density to model

Fig. 9 illustrates some of the complex issues related to the use of the pseudo-density. Fig. 9a (repeated from Fig. 6) shows the pseudo-density of He+, n_{He+}, along four radial cuts. Fig. 9b shows the model n_{He+} along the same cuts, under our assumption that the average ion mass is 1.4 amu, independent of L. The pseudo-densities for MLT = 3 and 6 and $L > 3$ represent noise rather than real signal, so the apparent difference between these densities and those of the model in the plasmatrough is not a problem. Similarly, the leveling off of the pseudo-density at very low $L < 2$ for MLT = 3 and 21 is due to the loss of signal in the Earth's shadow. Note, however, that there is a significant difference between the radial dependence of the

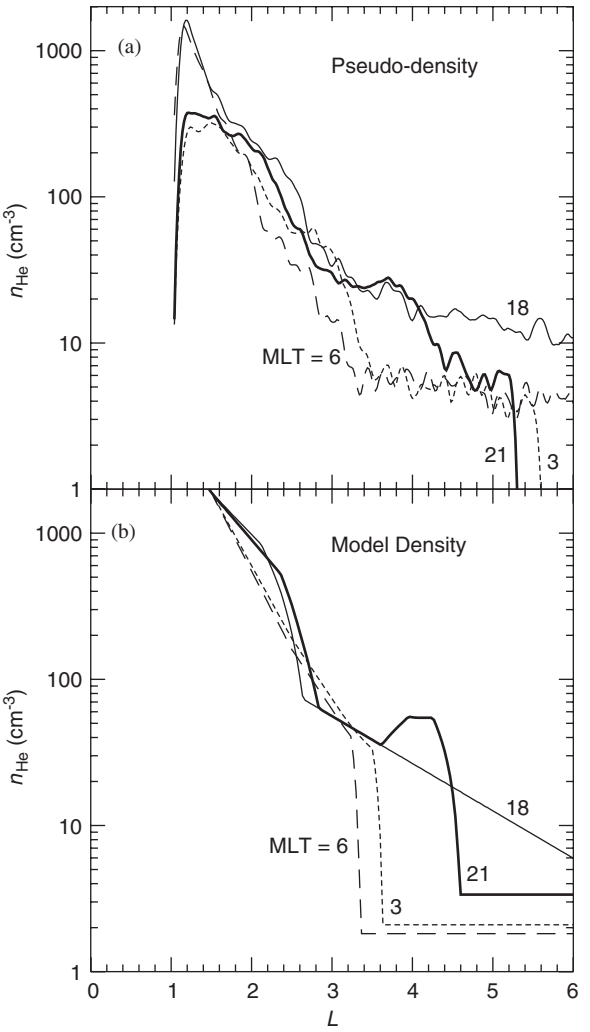

Fig. 9. (a) Pseudo-density of He+, n_{He}, versus L along four cuts, MLT = 18 (thin solid), 21 (thick solid), 3 (small dashes), and 6 (large dashes) (same as Fig. 6). (b) Model n_{He} along the same cuts.

pseudo-density and model density at MLT = 18. The pseudo-density at MLT = 18 is only slightly decreasing with respect to L for $L > 3$; roughly $\log_{10}(n_{He+})$ varies like $-0.17L$ in this region. From Craven et al. (1997) (their Eq. (2) with their Table 2), the value of $\log_{10}(n_{H+}/n_{He+})$ varies like $0.176L$. Then the L dependence at MLT = 18 implies (using the n_{H+}/n_{He+} ratio of Craven et al.) that n_{H+} should be approximately constant with respect to L. Such a dependence seems to be hard to reconcile with the dependence of mass density ρ in Fig. 7a, where ρ drops by close to two orders of magnitude between $L = 3$ and 8.

Another difference between Figs. 9a and b relates to the density cut at MLT = 21. In the model, there is a greater difference between the density in the plume at $L\sim4$ and the density just inside the plume then there is in the pseudo-density. A known problem with the pseudo-density inversion (as mentioned in Section 2.4) is that overdraping of high density plasma can lead to higher pseudo-density at lower L. Thus the real dip in density at about $L = 3$ may be greater than that shown in Fig. 9a, and a greater difference between the density in the dip and in the plume was necessary so that the plume be clearly visible in Fig. 8. Another problem concerns an increase in the EUV noise toward the dayside (Fig. 5). The combination of this with the dropout of signal on the nightside made it difficult to use the pseudo-density inversion to find the MLT dependence of the plasmatrough density. Because of these problems, we chose to use the pseudo-density only for some minor parts of the model, and depended mostly on the in situ RPI values and values of inferred mass density from the field line resonance mode.

3.4. Conclusions

We have demonstrated how a computer model for magnetospheric mass density can be constructed. The most important components of this model are the plasmasphere boundary (Section 2.2), the plasmasphere radial dependence (radial parts of (2) and (4)) and the radial part of the enhanced plasmatrough density (5), and these are the components of the model that are best based on observations. This model has been used to study the mechanism for Pi2 oscillations in the case of a small plasmapause (Kim et al., 2005). We have described some of the problems involved with EUV density inversion (Section 3.3), and have demonstrated some features of the plasmaspheric density, particularly in the region of the dusk plasmatrough and plume (Sections 2.1 and 2.5). The particular time examined here occurred about 15 h after a period of significant activity (Kp = 5.75, followed by Dst = −60), followed by a decrease in activity (Kp = 4) along with recovery of Dst (to −20). A plume such as the one observed here is frequently associated with an increase in activity, and may, like this one, wrap around the Earth toward the nightside when activity subsides (Goldstein and Sandel, 2005).

Acknowledgements

Work at Dartmouth was supported by NSF Grant ATM-0245664 and NASA Grant NAG5-11825. Work at UCLA was supported by NASA Graduate student research fellowship NASA NGT5-117. We thank the institutes who maintain the IMAGE magnetometer array. The authors thank the SAMNET team for providing the SAMNET and BGS magnetometer data. SAMNET is a PPARC National Facility operated by Lancaster University and BGS is a NERC funded facility.

References

Bauer, S.J., Stone, R.G., 1968. Satellite observations of radio noise in the magnetosphere. Nature 218, 1145–1147.

Benson, R.F., Webb, P.A., Green, J.L., Garcia, L., Reinisch, B.W., 2004. Magnetospheric electron densities inferred from upper-hybrid band emissions, Geophysical Research Letter 31, L20803, doi:10.1029/2004GL020847.

Berube, D., Moldwin, M.B., Weygand, J.M., 2003. An automated method for the detection of field line resonance frequencies using ground magnetometer techniques. Journal of Geophysical Research 108 (A9), 1348, doi:10.1029/2002JA009737.

Burch, J.L., Goldstein, J., Sandel, B.R., 2004. Cause of plasmasphere corotation lag. Geophysical Research Letters 31, L05802, doi:10.1029/2003GL019164.

Carpenter, D.L., Anderson, R.R., 1992. An ISEE/whistler model of equatorial electron density in the magnetosphere. Journal of Geophysical Research 97, 1097.

Craven, P.D., Gallagher, D.L., Comfort, R.H., 1997. Relative concentration of He+ in the inner magnetosphere as observed by the DE 1 retarding ion mass spectrometer. Journal of Geophysical Research 102 (A2), 2279–2289.

Denton, R.E., Gallagher, D.L., 2000. Determining the mass density along magnetic field lines from toroidal eigenfrequencies. Journal of Geophysical Research 105, 27,717.

Denton, R.E., Lee, D.-H., Takahashi, K., Goldstein, J., Anderson, R., 2002a. Quantitative test of the cavity resonance explanation of plasmaspheric Pi2 frequencies. Journal of Geophysical Research 107 (A7), doi:10.1029/2001JA000272.

Denton, R.E., Goldstein, J., Menietti, J.D., 2002b. Field line dependence of magnetospheric electron density. Geophysical Research Letters 29 (24), 2205, doi:10.1029/2002GL015963.

Denton, R.E., Goldstein, J., Menietti, J.D., Young, S.L., 2004. Electron density in the magnetosphere. Journal of Geophysical Research 109, A09215, doi:10.1029/2003JA010245.

Denton, R.E., Takahashi, K., Galkin, I.A., Nsumei, P.A., Huang, X., Reinisch, B.W., Anderson, R.R., Sleeper, M.K., Hughes, W.J., 2006. The distribution of density along magnetospheric field lines. Journal of Geophysical Research, submitted for publication.

Fraser, B.J., Horwitz, J.L., Slavin, J.A., Dent, Z.C., Mann, I.R., 2005. Heavy ion mass loading of the geomagnetic field near

the plasmapause and ULF wave implications. Geophysical Research Letters 32 L04102, doi:10.1029/2004GL021315.

Gallagher, D.L., Craven, P.D., Comfort, R.H., 2000. Global core plasma model. Journal of Geophysical Research 105, 18,819.

Gallagher, D.L., Adrian, M.L., Liemohn, M.W., 2005 Origin and evolution of deep plasmaspheric notches. Journal of Geophysical Research 110 (A9), A09201, doi:10.1029/2004JA010906.

Goldstein, J., Sandel, B.R., 2005. The global pattern of evolution of plasmaspheric drainage plumes. In: Burch, J.L., Schulz, M., Spence, H. (Eds.), Inner Magnetosphere Interactions: New Perspectives from Imaging. American Geophysical Union, Washington, DC, p. 1, doi:10.1029/2004BK000104.

Goldstein, J., Spasojevic, M., Reiff, P.H., Sandel, B.R., Forrester, W.T., Gallagher, D.L., Reinisch, B.W., 2003. Identifying the plasmapause in IMAGE EUV data using IMAGE RPI in situ steep density gradients. Journal of Geophysical Research 108 (A4), 1147, doi:10.1029/2002JA009475.

Goldstein, J., Sandel, B.R., Thomsen, M.F., Spasojevic, M., Reiff, P.H., 2004. Simultaneous remote sensing and in situ observations of plasmaspheric drainage plumes. Journal of Geophysical Research 109, A03202, doi:10.1029/2003JA010281.

Horwitz, J.L., Comfort, R.H., Chappell, C.R., 1984. Thermal ion composition measurements of the formation of the new outer plasmasphere and double plasmapause during storm recovery phase. Geophysical Research Letters 11 (8), 701–704.

Hughes, W.J., Southwood, D.J., 1976. Screening of micropulsation signals by atmosphere and ionosphere. Journal of Geophysical Research 81 (19), 3234–3240.

Kim, K.-H., Lee, D.-H., Denton, R.-E., Takahashi, K., Goldstein, J., Moon, Y.-J., Yumoto, K., Pyo, Y.-S., Keiling, K., 2005. Pi2 pulsations in a small plasmasphere. Journal of Geophysical Research 110, A10201, doi:10.1029/2005JA011179.

Laakso, H., Jarva, M., 2001. Evolution of the plasmapause position. Journal of Atmospheric and Solar Terrestrial Physics 63 (11), 1171–1178.

Luhr, H., Aylward, A., Bucher, S.C., Pajunpaa, A., Panjunpaa, K., Holmboe, T., Zalewski, S.M., 1998. Westward moving dynamic substorm features observed with the IMAGE magnetometer network and other ground-based instruments. Annals of Geophysics 16 (4), 425–440.

Menk, F.W., Orr, D., Clilverd, M.A., Smith, A.J., Waters, C.L., Milling, D.K., Fraser, B.J., 1999. Monitoring spatial and temporal variations in the dayside plasmasphere using geomagnetic field line resonances. Journal of Geophysical Research 104, 19,955.

Moldwin, M.B., Downward, L., Rassoul, H.K., Amin, R., Anderson, R.R., 2002. A new model of the location of the plasmapause: CRRES results. Journal of Geophysical Research 107 (A11), 1339, doi:10.1029/2001JA009211.

Reinisch, B.W., et al., 2000. The radio plasma imager investigation on the IMAGE spacecraft. Space Science Reviews 91, 319.

Roberts, W.T., Horwitz, J.L., Comfort, R.H., Chappell, C.R., Waite, J.H., Green, J.L., 1987. Heavy-Ion Density Enhancements in the Outer Plasmasphere. Journal of Geophysical Research 92 (A12), 13,499–13,512.

Sandel, B.R., King, R.A., Forrester, W.T., Gallager, D.L., Broadfoot, A.L., Curtis, C.C., 2001. Initial results from the IMAGE extreme ultraviolet imager. Geophysical Research Letters 28, 1439.

Sandel, B.R., Goldstein, J., Gallagher, D.L., Spasojevic, M., 2003. Extreme Ultraviolet Imager observations of the structure and dynamics of the plasmasphere. Space Science Reviews 109 (1–4), 25–46.

Schulz, M., 1996. Eigenfrequencies of geomagnetic field lines and implications for plasma-density modeling. Journal of Geophysical Research 101, 17,385.

Singer, H.J., Southwood, D.J., Walker, R.J., Kivelson, M.G., 1981. Alfven wave resonances in a realistic magnetospheric magnetic field geometry. Journal of Geophysical Research 86, 4589.

Takahashi, K., Denton, R.E., Anderson, R.R., Hughes, W.J., 2004. Frequencies of standing Alfvn wave harmonics and their implication for plasma mass distribution along geomagnetic field lines: statistical analysis of CRRES data. Journal of Geophysical Research 109, A08202, doi:10.1029/2003JA010345.

Takahashi, K., Denton, R.E., Anderson, R.R., Hughes, W.J., 2006. Mass density inferred from toroidal wave frequencies and its comparison to electron density. Journal of Geophysical Research, in press.

Tobiska, W.K., Woods, T., Eparvier, F., Viereck, R., Floyd, L., Bouwer, D., Rottman, G., White, O.R., 2000. The SOLAR2000 empirical solar irradiance model and forecast tool. Journal of Atmospheric and Solar Terrestrial Physics 62 (14), 1233–1250.

Tsyganenko, N.A., 1995. Modeling the Earth's magnetospheric magnetic-field confined within a realistic magnetopause. Journal of Geophysical Research 100, 5599.

Waters, C.L., Menk, F.W., Fraser, B.J., 1991. The resonance structure of low latitude Pc3 geomagnetic-pulsations. Geophysical Research Letters 18 (12), 2293–2296.

Wolf, R.A., 1995. Magnetospheric configuration. In: Kivelson, M.G., Russell, C.T. (Eds.), Introduction to Space Physics. Cambridge University Press, New York, NY, pp. 288–329.

Yeoman, T.K., Milling, D.K., Orr, D., 1990. Pi2 pulsation polarization patterns on the U-K subauroral magnetometer network (Samnet). Planetary and Space Science 38 (5), 589–602.